IEEE Access
Multidisciplinary | Rapid Review | Open Access Journal

Received 8 December 2023, accepted 7 January 2024, date of publication 11 January 2024,
date of current version 19 January 2024.

Digital Object Identifier 10.1109/ACCESS.2024.3353188

RESEARCH ARTICLE

A Broadband Inline Transition From On-PCB Microstrip to Hybrid Stack-Up Integrated Additively Fabricated Air-Filled Waveguide

JAKUB SOROCKI[1], (Senior Member, IEEE), ILONA PIEKARZ[1], (Senior Member, IEEE), NICOLO DELMONTE[2], (Member, IEEE), LORENZO SILVESTRI[2], (Member, IEEE), AND MAURIZIO BOZZI[2], (Fellow, IEEE)

[1]Institute of Electronics, AGH University of Krakow, 30-059 Kraków, Poland
[2]Department of Electrical, Computer and Biomedical Engineering, University of Pavia, 27100 Pavia, Italy

Corresponding author: Jakub Sorocki (jakub.sorocki@agh.edu.pl)

This work was supported by the National Science Centre, Poland, under Grant 2019/34/E/ST7/00342.

ABSTRACT A novel type of a highly integrated low-loss stack-up is explored that leverages additive manufacturing for the integration of a 3D printed and metal-coated air-filled waveguide with a Printed Circuit Board (PCB) by sharing a common ground plane. A complementing microstrip to waveguide transition is proposed exploiting the flexibility of the 3D printing technology to realize an in-line E-field and smooth profile continuous impedance transformation to ensure low insertion losses, wideband operation, and high return loss. Field mode matching and monotonic impedance profile are ensured using various intermediate guides along with the transition. A fast design procedure relies on analytical expressions for guides' impedance that was proven not to require further full-wave model optimization. The concept was experimentally validated by the realization of demonstrators operating within the cm- and mm-wave frequency range and fabricated employing a subtractive PCB and additive vat photopolymerization 3D printing and copper plating technologies. A hybrid WR-90-sized waveguide with RMS metal coating roughness of 1.5 μm yields power loss below 0.026 dB/cm being comparable to an all-metal counterpart. Measured back-to-back half-wavelength long at lower cutoff transitions to either WR-90 or WR-28 hybrid waveguides operate with bandwidth of $\sim$1.9 and $\sim$1.4 (return loss better than 10 dB) with 0.63 dB and 0.86 dB average loss per transition within 8.2 – 12.6 GHz and 26.5 – 40 GHz bands, respectively.

INDEX TERMS 3D printing, additive manufacturing, broadband transition, metal coating, microwave, waveguide, PCB technology, transmission line.

I. INTRODUCTION

The increasing growth of wireless and RF technologies observed in many applications requires new solutions enabling novel designs featuring low-loss and compact size as well as featuring reduced waste and considerable cost-saving in high-volume production. Additive Manufacturing technology (AM), initially adopted for rapid prototyping to test the design before the final product development, recently evolved towards end-use components [1], [2], [3], [4], [5]. This is due to the significant improvements in the manufacturing equipment and material engineering, but also due to the design flexibility it provides. AM technologies allow for the realization of various passive waveguiding structures [5], [6], [7], [8], which can feature lower losses due to the presence of air dielectric than currently used Substrate Integrated Waveguides (SIW), in which the electromagnetic wave propagates fully [6], [7], [8], [9], [10], [11] within the

The associate editor coordinating the review of this manuscript and approving it for publication was Giovanni Angiulli.

lossy dielectric substrate. Moreover, the performance of such AM components is comparable to industry standard all-metal waveguides with the superior benefit of reduced material and fabrication cost, reduced weight, unprecedented 3D geometry flexibility, and high-integration possibilities. Nevertheless, a fabrication and an assembly scheme that takes advantage of both AM and PCB technologies on which it is possible to have active circuitry are strongly desired and it requires to design of appropriate transitions. Recently, examples of such low-loss circuits have been introduced that are Empty-SIW (E-SIW) type [12], [13], [14] structures in hybrid stratification where a 3D printed dielectric insert introducing air cavity inside the guide is sandwiched between two laminates with either etched metal pattern [15] or laser-structured thick metal sheets [16], all stitched with non-PCB-standard vias/rivets. The downside of the above is that those are still planar structures not far from classic PCB SIWs, however, no longer require precise laminate milling as this is the case for all-in-PCB Air-filled SIW (AF-SIW).

In the literature, different metallic waveguides to PCB transitions can be found e.g., inline ridge stepped transformer [17], [18], quasi-Yagi [19], probe-feeding [20], slot coupling [21], patch-coupling type [22], inline guide stepped transformer [23], [24]. The realizations presented in [17], [18], and [19] require the insertion of PCB into the waveguide, however, offer in-line transition with multi-step impedance transformation. The drawback of probe-feeding [20] is the need for the radiating post inside the waveguide. The transitions shown in [21] and [22] require vertical orientation of waveguide which is not suited for highly integrated circuits such as additively fabricated air-filled waveguide integrated with a printed circuit board hosting a strip transmission line. The transitions shown in [23] and [24] require down and up impedance transformation due to the intermediate guide.

In this paper, we explore and study in detail a novel type of highly integrated low-loss stack-up, introduced in [25] and further developed in [26], that leverages additive manufacturing for integration of a 3D printed and metal-coated air-filled waveguide with a strip transmission line. The proposed realization offers high three-dimensional flexibility with a Printed Circuit Board (PCB) hosting microstrip guide by sharing a common on-PCB metal plane yielding a parallel guide arrangement. In [25] the stack-up idea was only briefly described along with a relatively simple through-patch transition between guides, i.e., from microstrip transmission line to rectangular waveguide featuring a limited bandwidth and fairly high losses. In [26] an effort was made to improve the transition properties by introducing a through-radiation probe transition where a selectively metalized 3D-printed post was used improving both the bandwidth and losses. Nevertheless, both transitions rely on resonant coupling mechanisms that pose a limit on bandwidth and cause excessive radiation losses due to extra on-PCB open-ended microstrip resonators that are necessary to extend the bandwidth. This

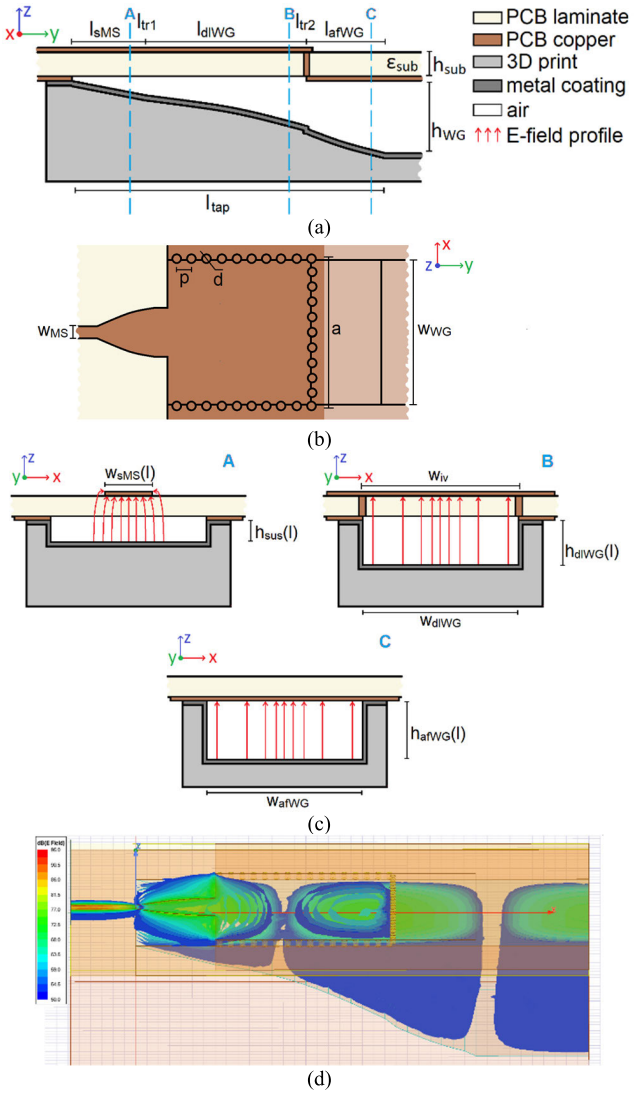

FIGURE 1. The side, top, and front cross-sectional views of the transition at (a) X-, (b) Z-, and (c) Y- cut planes with main geometry parameters indicated and E-field orientation for the dominant mode marked. Wave propagation along the Y-axis from microstrip to an air-filled waveguide with three distinctive intermediate guides providing a quasi-TEM mode in the suspended microstrip region - A and TE10 mode in the dielectric-loaded waveguide - B and air-filled waveguide - C. (d) Full-wave simulated E-field field distribution within an exemplary transition (see Sec. IV.C for more details).

is not to mention the relatively large space occupied on top of the on-PCB metal layers and/or more sophisticated AM fabrication.

To overcome the above issues and to take advantage of the full bandwidth potential of the proposed integrated waveguide, a complementing microstrip to waveguide transition is proposed exploiting the flexibility of the 3D printing technology to realize an in-line E-field and smooth profile continuous impedance transformation as to ensure low insertion losses, wideband operation, and high return loss. The added benefit is a transition's compact size on the microstrip side as for most of the transition length, only the ground plane

is needed making room for on-PCB circuitry. A fast design procedure is developed producing the transition geometry with a given impedance taper using only analytical expressions for each intermediate guide that was proven not to require further full-wave model optimization. A detailed discussion of the AM fabrication aspects covering requirements and limitations and the impact of the selected fabrication scheme on the circuit performance is provided.

Moreover, transition demonstrators operating within the X- and Ka-band are fabricated employing a subtractive PCB and additive vat photopolymerization 3D printing and copper plating technologies to validate the design procedure. The obtained results for transitions to WR-90 and WR-28 waveguides having full-wave non-optimized geometry where almost full single-mode bandwidth of the waveguide is covered certify the advantages and applicability of the proposed approach towards mm-wave circuits realization.

II. ON-PCB MICROSTRIP TO AIR-FILLED WAVEGUIDE TRANSITION

The idea of the integration of a U-shaped additively fabricated air-filled waveguide with the PCB hosting a strip transmission line was introduced in [25]. The waveguide structure is realized as a U-shaped element with a metal coating on the inside three walls, whereas the fourth metal wall is created by the ground plane of the attached PCB. Such a realization features significant design flexibility since part of the elements can be realized using a waveguide and part can be attached and/or etched on PCB. Moreover, power losses are minimized as an air-filled guide is available. Such an approach is a step beyond the industry standard stack-up where a microwave substrate hosting SIW structure is attached to a multilayer PCB, towards a more feature-packed next generation of cm- and mm-wave systems realization technology.

To take advantage of the full potential of the proposed integrated stack-up, a complementing broadband transition between the guides was developed. The concept relies on the implementation of a continuous taper impedance transformer with such intermediate guides arrangement that ensures propagation modes matching. To transform from the microstrip impedance to one of the air-filled waveguides, various taper functions such as Klopfenstein [27] or Chebyshev [28] can be used depending on the required response properties. Apart from the input/output guides, intermediate guides are introduced with partial or full air filling having a matched inline E-field orientation to smoothly transition from the quasi-TEM to TE mode, namely: suspended microstrip (sMS), dielectric-loaded waveguide (DL-WG), and air-filled waveguide (AF-WG). A given impedance taper is implemented in transition geometry mainly by varying the air layer thickness along the transition length which is easily done in the metal-coated 3D-printed part of the assembly. The above ensures wideband operation with low insertion and high return losses. From the transmission line standpoint, the proposed transition is a uniform and matched transmission line section as no impedance discontinuity is introduced even though various guides are used along its length. For that reason, no EM-based optimization is necessary thus benefiting the proposed approach with a significantly reduced time-to-design.

A. TRANSITION CONSTRUCTION

General views of the proposed transition are provided in Fig. 1. The first intermediate guide is a suspended microstrip (see Fig. 1c, cross-section A) supporting a quasi-TEM wave. This is due to the following reasons. Direct transitioning from a quasi-TEM microstrip to a TE waveguide type structure such as SIW, even as it might appear to be attractive, poses an issue on the realization of a monotonic impedance profile. The wave impedance of an SIW is relatively low (in the range of 10 Ω to 50 Ω) and depends on the PCB's substrate thickness and permittivity (for a fixed cut-off frequency), thus neither impedance of 50 Ω and higher, nor impedance tapers could be achieved. Subsequently, a dielectric-loaded air-filled waveguide (see Fig. 1c, cross-section B) would require a thin air layer to realize an impedance of 50 Ω or slightly higher. In this case, the effective permittivity of such guide filling changes rapidly with small increments in thickness, thus it would be very sensitive to the fabrication tolerances. On the other hand, the suspended microstrip can realize the desired impedance taper with a smooth launch from the microstrip input starting from 50 Ω upwards leveraging the air layer profile to a benefit. The (suspended) microstrip top conductor is etched on PCB while the ground plane beneath is realized by the metal-coated 3D printed element enabling a gentle taper along the transition length l towards a fully open air-filled waveguide at $l = l_{tap}$. The microstrip transmission line having a width of w_{MS} transitions to a suspended microstrip line having a width of $w_{sMS}(l)$ at $l = 0$. The characteristic impedance depends upon the top conductor width and suspension height (for a given PCB dielectric). The suspended line length of the transition l_{sMS} can be designed in a way that the transition to a dielectric-loaded waveguide DL-WG at $l = l_{tr1}$ is at its widest top conductor point (while maintaining the given impedance tapers $Z_{tap}(l)$). For this part, the suspension height is assumed to increase linearly with l (h_{sus} @ $l = l_{tr1}$ is found to match the DL-WG h_{WG} @ $l = l_{tr1}$) while the strip width profile $w_{sMS}(l)$ is found as described in the following subsection.

Transitioning at $l = l_{tr1}$ from the suspended microstrip minimizes the top metal width change as when changing the guide type to a DL-WG. Moreover, at this point, the $h_{sus}(l_{tr1})$ the effective permittivity of the DL-WG (air-layer height dependent) converges to a value close to unity. As indicated earlier, since DL-WG supports TE wave, it features a lower cut-off frequency that depends on the waveguide width and air-layer height (for a given PCB dielectric) so the wave impedance does. Considering that the effective permittivity is not going to vary much past l_{tr1}, one can assume a fixed width of the DL-WG $w_{WG}(l)$ that matches one of the output AF-WG that yields f_c ignoring a small cut-off frequency variation as such assumption reduces the problem in finding the geometry profile of air-layer height $h_{dlWG}(l)$ only. It is worth noting that

for the SIW-alike part of the AF-WG, the via spacing on the PCB that connects to the metal-coated part is set to yield an effective width of w_{WG}. The DL-WG transitions to a variable air-layer height air-filled waveguide at $l = l_{tr2}$ and being l_{dlWG} long. End-shorting via fence (realized similarly as the sides shorting via fences) is placed at l_{tr2} to connect the top metal with the ground plane that constitutes the waveguide broad wall.

The air-filled waveguide features no dielectric loading and thus its wave impedance depends upon its height $h_{WG}(l)$. Therefore, a realization of the remaining impedance taper requires finding the narrow-wall height profile $h_{afWG}(l)$ while keeping the $w_{WG}(l)$, similarly as for the previous guide fixed and equal to the output AF-WG to reach $h_{WG}(l_{tap}) = h_{WG}$. The intermediate AF-WG guide has a total length of l_{afWG}.

B. DESIGN PROCEDURE

Subsection A discusses the transition arrangement while the Appendix provides analytical formulas for impedances of each transmission line type involved. Guides' geometry is calculated at each discrete point along the taper length by solving numerically an inverse problem for a given impedance and current guide type. Therefore, a specific design procedure for the proposed transition can be formulated as follows:

First, the PCB substrate is selected (material and thickness) considering, among others, the intended frequency range of operation to ensure the propagation of the (quasi)TEM-mode only in the microstrip guide. The input/output microstrip impedance Z_{MS} is established followed by determination of the line's width w_{MS}.

Next, the transition's center frequency of operation is selected, which is necessary to establish the waveguide's cut-off frequency. The accepted limits of operation of the fundamental mode for a rectangular waveguide are (approximately) between 125% and 189% of the lower cut-off frequency $f_{c\mathrm{TE10}}$. Thus, for the center frequency of operation f_0 to be in the middle of the above, the waveguide's cut-off frequency should be $f_{c\mathrm{TE10}} = f_0/1.575$.

Having the above, the waveguide's broad-wall width w_{WG} is calculated [28] while fixing $\varepsilon_{eff} = 1$. This is followed by selecting the input/output AF-WG narrow-wall height h_{WG}. It must be noted here that the proposed transition bandwidth is limited by the single-mode operation of the AF-WG that depends on the broad wall-to-narrow wall relation. Moreover, only the $\mathrm{TE_{X0}}$ modes can be excited in the proposed transition arrangement due to the feed line E-field orientation. For a case where $h_{WG} \leq w_{WG}/2$, a single-mode operation spans across the $\mathrm{TE_{10}}$ and $\mathrm{TE_{20}}$ modes up to $\mathrm{TE_{01}}$ mode cut-off (defined by h_{WG}), hence lower the height, the broader the bandwidth. On the other hand, for $h_{WG} \geq w_{WG}/2$ the bandwidth is reduced to one of the $\mathrm{TE_{10}}$ mode as the $\mathrm{TE_{01}}$ mode becomes the 2^{nd} mode. Finally, the AF-WG impedance Z_{WG} is calculated using (A.4). It is important to note that the wave impedance is frequency dependent. However, assuming $f = f_0$ and using a single value for the sake of the design does not come with a significant transition performance deterioration while it simplifies the procedure. The above applies to all impedance points across all TE guides.

Following, the impedance taper function is selected and the discrete impedance transformation profile from Z_{MS} to Z_{WG} is calculated. The number of points is selected considering fabrication capabilities and smoothness of the function as well as the XY and Z resolution of the 3D printer of choice. Simulation results have shown that discretization in the range of 30 to 120 points is sufficient depending on the total transition length.

A coarse transition length is determined to be half the wavelength for an AF-WG of selected width at the required lower cut-off frequency being $f_{cl} = 1.25 f_{c\mathrm{TE10}}$. The initial geometry might not provide exactly the desired passband, however, is required to establish the actual one once the geometry-dependent guide's effective permittivity is determined by calculating the phase shift along the transition. The length can then be fine-tuned to obtain the specified cut-off f_{cl}. For example, for the Klopfenstein taper, the in-band phase shift must be higher than 1.13π.

The geometry profile for the suspended microstrip region is calculated and the optimum length l_{sMS} is established by cross-referencing to a geometry profile for DL-WG. Simulation results have shown that the optimum length of the sMS guide is roughly a quarter of the total length. The geometry profile for DL-WG is calculated and its length l_{dlWG} is selected. In both cases (sMS and DL-WG), the effective permittivity is higher than unity, and thus the longer they are, the lower transition's cut-off frequency for a given physical length. Simulation results have shown that for lengths greater than roughly half of the total transition length little to no cut-off frequency lowering is observed. On the other hand, for a shorter DL-WG section, less space is occupied on the microstrip guide side of the PCB with the corner case being no DL-WG section at all. Fixed waveguide broad-wall width is used and corresponding via spacing a of the on-PCB SIW-alike structure is calculated accordingly [29] considering that via pitch p and via diameter d should fulfill inequalities $d < 0.1 w_{WG}$, $p < 2d$ as to minimize power loss due to radiation through the via fence. Finally, the geometry profile for air filled waveguide region is calculated for the remaining length of the transition.

A MATLAB script (available at www.microwaves.agh.edu.pl) was developed to automatically calculate the transition geometry profiles for a given impedance taper and to generate a Computer-Aided Design (CAD) file that is imported to a Computer-Aided Manufacturing (CAM) software for fabrication. The same file can also be easily imported to a full-wave EM solver for design verification and optimization if needed. The performance of such analytically synthesized transitions was experimentally tested by exemplary designs presented in the subsequent Section.

III. FABRICATION AND EXPERIMENTAL RESULTS

PCB-integrated waveguide along with the proposed broadband transition was experimentally validated. An exemplary hybrid fabrication scheme that employs PCB and AM technologies is introduced and its affection on the circuit's performance is discussed along with technological requirements and limitations. An exemplary waveguide section was developed to validate the fabrication process along with exemplary transitions to validate the performance of the proposed analytical geometry synthesis approach. Demonstrators are designed to operate within the cm- and mm-wave frequency range to assess the synthesis scalability with increasing frequency and fabrication scheme usability with decreasing dimensions. Standard WR-90 sized ($w_{WG} = 22.86$ mm, $h_{WG} = 10.16$ mm; TE_{10} mode accepted band from 8.2 GHz to 12.4 GHz, center frequency of $f_{0\_WR90} = 10.5$ GHz) and WR-28 sized ($w_{WG} = 7.11$ mm, $h_{WG} = 3.56$ mm; TE_{10} mode accepted band from 26.5 GHz to 40 GHz, center frequency of $f_{0\_WR28} = 33.25$ GHz) waveguide geometries were adopted for the designs as they provide a broadband single-mode operation of TE_{10} and TE_{20} modes with wavelengths ranging from 60.9 mm to 8.8 mm. The same fabrication equipment and process were used for both bands.

Scattering parameters of all circuits were measured using the Agilent PNA N5224A vector network analyzer capable of collecting data within the 10 MHz to 43.5 GHz range at IF bandwidth of 1 kHz and 10 MHz step with the calibrated reference plane set at either waveguide flange (A-Info WR-90 TRL cal-kit) for waveguide testing or coaxial connector (Agilent coax SOLT cal-kit) for transitions testing.

A. CIRCUITS' FABRICATION AND ASSEMBLY ASPECTS

The selection of technologies, processes, and assembly techniques used for the fabrication of the proposed circuits must be done considering the intended frequency range of operation. This is due to the requirements they must fulfill. In general, as frequency increases the smaller guide and feature sizes become hence higher fabrication resolution is needed as well as shallower current skin depth becomes so a smoother metal surface is required to minimize conductor losses. A rule of thumb for PCB fabrication can be adopted that mask resolution should be 10 to 20 times higher than the minimum feature size. This varies with other factors such as etching and drilling accuracy or pattern complexity. A rule of thumb for AM fabrication can be adopted that 3D printing resolution should be 50 to 100 times higher than the guided wavelength of the highest frequency of operation. This varies with other factors such as the type of printing technology or geometry complexity. On the other hand, metal surface roughness should not exceed skin depth at the highest frequency of operation as when RMS roughness is approximately equal to skin depth, conductor loss is increased by 60% [30]. When roughness is much higher than the skin depth, conductor loss is 2 times higher (100% increase) compared to loss under ideal smooth metal conditions.

The following scheme was used for manufacturing the experimental circuits:

The printed circuit boards were fabricated in-house using an industry-standard PCB process. Either 20 mils (X-band circuits) or 12 mils (Ka-band circuits) thick Rogers RO4003C laminate was used with double-sided copper-clad (17 μm thick foil, RMS roughness of 0.4 μm for top side (affecting waveguide) and 2.6 μm for dielectric side (affecting microstrip)) having process permittivity of 3.38 and loss tangent of 0.0027, both @ 10 GHz ($\varepsilon_{sub} = 3.5$ was assumed for the design as of Authors experience with the material). Metal traces were fabricated using photolithography technology, i.e., the on-laminate copper is coated with a UV-sensitive photoresist that is exposed through a mask with the pattern (here 2540 dpi Computer to Film print) so the un-mask metal can be chemically etched. The DL-WG via fence features $d = 0.5$ mm and $s = 1$ mm. Holes were drilled on a drill press and positioned by on-PCB drill guides. The through-hole vias were metalized using a conductive silver paste. A study was conducted for the perpendicular via-fence at DL-WG to AF-WG transition properties affection (EM TR-B transition model used, see Section 3.3.1 for references) revealed that the denser the via fence the lower power losses. Increasing both d and p by 100% w.r.t. the above used leads to 5% @ f_{0_WR90} power loss increase while by 200% to 28% @ f_{0_WR90} increase. Moreover, metal on the top plane must only extend by 1 mm or so past the via diameter to maintain the minimal losses and thus further extension is not needed.

The 3D waveguide parts were fabricated in-house in a two-step process. At first, the plastic shells were 3D printed using the Masked Stereolithography (M-SLA) technology out of Siraya Tech Fast ABS-like Smoky Black UV-cured resin (post-curing shrinkage 1.5-2% per axis) using the Prusa Research Original Prusa SL1S printer with 50 μm XY-resolution (high-resolution monochrome LCD panel) at 50 μm layer height (min. 25 μm). A (semi)transparent print is convenient for further fabrication and assembly steps. This was followed by conductive coating fabrication. The electroplating process out of the electrolyte bath was used to grow roughly a 5 μm thick copper layer (current skin depth $\delta = 0.64$ μm @ f_{0_WR90} assuming bulk copper conductivity). Since the parts were non-conductive, a conductive base layer was painted using the silver-based LPKF ProConduct Paste targeting roughly 20 μm film thickness. An added benefit of the base layer is the potential reduction of bare-print surface roughness due to the printing process. It must be noted that the paint thickness uniformity, hence surface resistance affects the current density uniformity and thus the plated layer thickness uniformity and roughness. It is important as mating two rough metal surfaces may result in a non-uniform galvanic contact leading to distorted current distribution and thus increased power losses.

The two-part construction was then assembled. A set of corresponding holes was placed on the PCB and the 3D printed part to accept the alignment pins which in this case were M2 screws serving a double purpose, i.e., fixing the

XY position of the parts and providing a pressure-assisted low resistance contact between the on-PCB ground plane and waveguide top contact metals. Such a solution was adopted to minimize contact resistance which is one of the major contributing factors to the total power losses of the circuits. The effect is more pronounced as metal surfaces mate in waveguide regions of higher current concentration, mainly in the MS to sMS launch region and secondarily in the WG narrow and broad wall seam. A rule of thumb was adopted for the design so that the minimum pitch between screws should be roughly lower than 0.4 times the waveguide's broad wall (here 8 mm screw pitch for WR-90 and 3 mm for WR-28, 2 mm screw holes used). This also allows us to minimize the negative influence of potentially appearing air gaps, i.e., power leakage or broken current paths. Such gaps are most likely to appear because of uneven pressure holding the parts that are a result of either too low clamping force if 3D print integrated clips are used or too high pointwise clamping force if screws or metal clips are used at too large intervals causing the PCB to deform, creating high-low or high-no clamping pattern. Moreover, the mechanical integrity of the parts must be considered as well (minimal wall thickness of the print, minimal inter-hole distance of the PCB) limits the pitch. In general, a different scheme can be used, and the above two functions can be separated. A set of 3D part integrated posts and corresponding on-PCB holes could be used to enforce alignment which when using more than two per transition also minimizes the fabrication tolerances affection on alignment. On the other hand, an assembly connection mechanism featuring a distributed force type of contacts such as 3D-print integrated springs or clamps could be used, as studied in [31].

Finally, the applicability of the above-described fabrication procedure towards mm-wave circuits fabrication and upper frequency limitation due to resolutions available is assessed. This is of great importance as usually waveguides are used in the mm-wave range to mitigate dielectric losses and provide a low-loss guide. Considering the rule of thumb requirements provided in the first paragraph, the following can be established:

PCB fabrication – feature size: the used photolithography technology provides a resolution of 10 μm which translates to feature size in the minimal range of 100 μm to 200 μm. The above is sufficient for circuits operating roughly up to E-band (60 - 90 GHz).

PCB fabrication – via fence: the specified via diameter and pitch used is at the limit of the used fabrication technology. To keep radiation losses minimum the realized fence is sufficient for a waveguide broad wall as narrow as roughly 5 mm. The above aligns with standard waveguide size down to WR-19 (40 - 60 GHz)

AM fabrication – polymer shell: the used vat photopolymerization technology provides a resolution of 50 μm in X, Y, and Z-axis which yields upper wavelength limitation in the range of 2.5 mm to 5 mm. The above is sufficient for circuits operating roughly up to V-band (75 - 110 GHz). This is however dependent also on the viscosity of the used resin as well as the shape and size of features with small ridges, groves, irises, or chambers requiring particular attention.

AM fabrication – metallization: measured RMS roughness of the fabricated conductor is around 1.5 μm (see. Section II-B). Skin depth for pure copper at 50 GHz is 0.3 μm while for 100 GHz drops to 0.2 μm which is 5 to 7 times the roughness. Thus, increased losses can be expected, however, those could be reduced when using a different metallization technique.

Assembly – contact resistance: for the sake of this study, the two-part assembly was connected using screws. For the used screw hole size, a minimal pitch of roughly 3 mm is required to maintain mechanical integrity. The above aligns with standard waveguide size down to WR-28 (26.5 - 40 GHz), however, if increased contact resistance is acceptable then this could be further pushed roughly down to WR-19. To mitigate this issue, different assembly methods could be used as discussed earlier. Alternatively, the mating metal faces could be soldered together with low-temperature soldering to create a reliable and low-resistance connection pushing higher the frequency of operation.

In summary, the upper frequency limit of the fabrication scheme usability is a combination of the above factors coupled with assembly accuracy. In the next subsections, the proposed scheme is experimentally tested for circuits up to mm-wave frequency range. Importantly, a higher frequency of operation requires tighter tolerances as the geometrical dimensions scale down, otherwise, the fabricated circuit performance deteriorates.

B. PCB-INTEGRATED ADDITIVELY FABRICATED AIR-FILLED WAVEGUIDE

At first, a section of a PCB integrated waveguide was developed featuring WR-90 geometry with the main objective to establish the geometry accuracy and power losses of such a guide for the used fabrication scheme. A transition from a short section of a regular waveguide with a standard WR-90 flange to the hybrid guide was added at each end to enable S-parameter measurement. To minimize the impact of the above transitions, the hybrid section was made at least 10 times longer. A 120 mm long guide test unit was fabricated (5 mm per flange, 110 mm of hybrid waveguide) out of which a test piece was cut out (after completing electrical characterization, a metal surface parallel to printer's screen) as for metal profile inspection.

The experimental results were collected. First, the mechanical properties of the AM-fabricated test piece were assessed. Dimensions of the part were measured using a digital caliper (10 μm least significant digit) to assess the fabrication tolerance including resin curing-related shrinkage and metal coating. The inner geometry, i.e., waveguide cross-section and length are 22.77 mm (aligned with printer's screen XY plane) by 9.74 mm (aligned with printer's stage movement) by 119.54 mm (aligned with printer's screen XY plane) which

is a deviation by 0.4%, 4%, and 0.4%, respectively from the designed dimensions. Waveguide height is more prone to human error as here it is a depth measurement. On the other hand, an off-the-shelf all-metal waveguide reference sample measured 22.85 mm by 10.16 mm at internal cross-section which is aligned with the WR-90 specification.

Then the Bruker Dektak XT stylus profilometer was used to assess the surface profile. The total coating thickness was established to be roughly 15 μm. Considering the overall waveguide dimensions, the coating thickness has hardly any affection on performance due to the dimensions change. The waviness-corrected RMS metal roughness *Rq* for the tested sample at a 5 mm long path was measured to be 1.5 μm while the RMS surface roughness that includes long wavelength effects was 5.2 μm. The resulting metal roughness indicates that increased power losses (as compared to smooth metal) are to be expected (effective metal conductivity is reduced at least 2 times as compared to bulk metal value). Moreover, since the low-roughness PCB metal plane comprises only one of four waveguide broad walls, the electroplated metal contributes the most to total power loss.

Following, the S-parameters were measured for the fabricated hybrid waveguide and the reference all-metal sample. The data was processed, and total power loss (TPL) was calculated as $TPL = 1 - \left(|S_{21}|^2 + |S_{11}|^2\right)$ which for a well-matched circuit simplifies to $TPL \approx 1 - e^{-2\alpha l}$ where $\gamma = \alpha + \mathrm{j}\beta$ is the guides‘ propagation constant while α and β are attenuation and phase constants, respectively. Since very low losses are measured, the VNA-related uncertainty of $|S_{21}|$ measurement cannot be overlooked as the results are of the same order of magnitude, here test sample length scale uncertainty equals 0.02 dB [32]. Assessing the results, very low losses that average at 0.026 dB/cm within WR-90 bandwidth were obtained for the proposed hybrid waveguide which is comparable to 0.007 dB/cm for the reference sample. The resulting structure‘s available unloaded quality factor Q_u, which is of importance from a filter realization standpoint, for the test sample, is roughly 28% of this for an all-metal waveguide. It is important to note, however, that both the WR-90 mating flanges (relatively rough mating surface) and regular to hybrid waveguide transitions (resistivity of contact between coated metal and on-PCB metal plane) that are integrated within the test unit cause extra losses that overstate the above figures. Finally, cut-off frequency was determined for both waveguides yielding 6.549 GHz for the hybrid and 6.577 GHz for the all-metal one. Affecting factors are both dimensional and power loss (attenuation constant) differences.

Finally, a full wave model of the fabricated hybrid guide was built and simulated in the *Ansys HFSS* software to assess and separate the power loss sources; Groisse roughness model used. The model yields losses of 0.0036 dB/cm @ f_{0_WR90} when the on-PCB metal is smooth copper while the AM metal coating has conductivity of 10 MS/m with roughness of 5 μm which is similar to one of the all-metal reference made out of aluminum alloy (conductivity of 20 MS/m, roughness of 1 μm, loss of 0.0038 dB/cm @ f_{0_WR90}). When using printing and metallization technologies that yield high-quality metal surfaces, waveguide losses are in the range between 0.0017 dB/cm (conductivity 50 MS/m, roughness 0.5 μm) and 0.0027 dB/cm (conductivity 20 MS/m, roughness 2 μm). Considering the above in terms of unloaded quality factor would yield Q_u between 4500 and 2800 @ f_{0_WR90}. When between mating metal surfaces a 50 μm thick layer having a sheet resistance of 0.02 Ω/sq is added that models contact resistance, the loss increases by another 0.01 dB/cm @ f_{0_WR90}. Thus, to improve the loss performance, the contact quality between the metallic surfaces could be optimized, e.g., using softer metal or an interposer followed by improvement of metal layer conductivity and/or reducing surface roughness optimizing the presented process or using, e.g., one studied in [33] or described in [34]. Nonetheless, the employed fabrication process yields good results and serves well the purpose of further validation of the proposed transition construction and synthesis method.

C. HYBRID FABRICATED MICROSTRIP TO AIR-FILLED WAVEGUIDE TRANSITION

Secondly, exemplary broadband transitions from an on-PCB microstrip to an integrated waveguide were designed: one into WR-90 sized waveguide, namely TR-90, and another into WR-28 sized one, namely TR-28 with the main objective of validating the developed design and geometry generation algorithm. The lower cut-off frequency of the taper was assumed to match roughly the waveguide‘s accepted lower limit of operation. A Klopfenstein taper $Z_{tap}(l)$ was generated for return loss of 25 dB at N = 90 discrete points to transform the impedance from $Z_{MS} = 50\ \Omega$ to $Z_{WG\_WR90} = 265\ \Omega$ in case of TR-90 and to $Z_{WG\_WR28} = 297\ \Omega$ in case of TR-28. Transitions‘ physical length of $l_{tap\_WR90} = 30.4$ mm (half wavelength at 8.3 GHz) was assumed in the case of TR-90 and $l_{tap\_WR28} = 9.3$ mm (half wavelength at 26.5 GHz) in the case of TR-28. Even though the use of a DL-WG section has the benefit of a lower cut-off for the same physical length, the reduced transition arrangement with no DL-WG section was used. Such configuration presents a few benefits: - reduces the area occupied by the transition at all except very bottom (used as waveguide broad wall) on-PCB metal layers making room for other active or passive circuitry, - reduces the fabrication effort as DL-WG related on-PCB side via-fences are no longer required, - eliminates the DL-WG related dielectric and radiation losses. Thus, for both transition demonstrators the first intermediate guide transition was set close to the widest point of the sMS width while the second one was set at same distance to skip the DL-WG guide, hence $l_{tr1} = l_{tr2} = 0.27 l_{tap}$ was assumed. The developed MATLAB script was used to generate transitions‘ geometry and the resulting profiles are shown in Fig. 2.

Transitions‘ frequency response was verified using a full-wave transition model in *Ansys HFSS* software where the

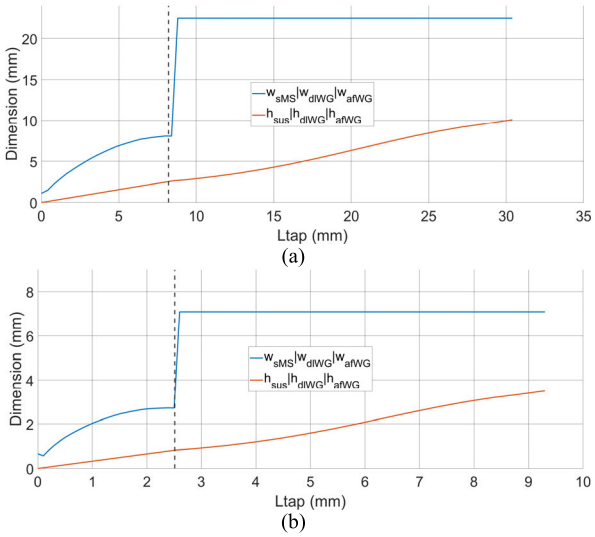

FIGURE 2. Generated geometry profile for the (a) TR-90 and (b) TR-28 transition. Guides transition marked (vertical dashed line); no DL-WG guide.

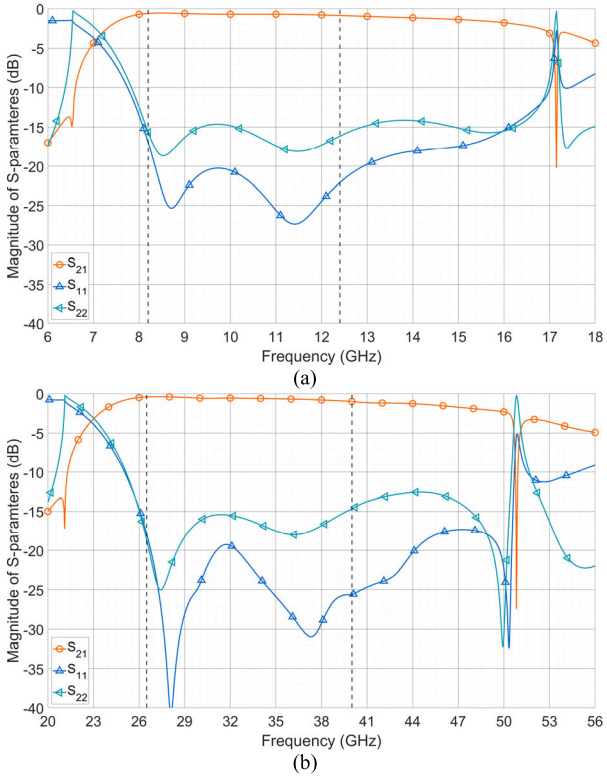

FIGURE 3. EM calculated frequency response of the (a) TR-90 and (b) TR-28 transition. Port #1 is the microstrip side, #2 is the waveguide side. WG TE10 bandwidth marked (vertical dashed lines).

waveguide body was simulated as a full-metal element with a conductivity of copper and smooth surface; lossless contact between on-PCB plane and waveguide seam was set; lossy laminate properties as of RO4003C specification were set. As seen, broadband operation is obtained within the specified frequency range with the lower cut-off roughly as required. Impedance match (microstrip side) is better than 20 dB and

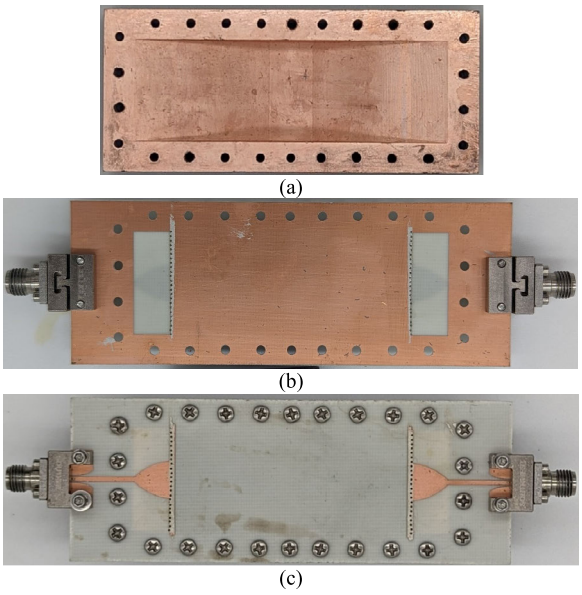

FIGURE 4. Photographs of the fabricated TR-90 transition in back-to-back configuration: (a) copper-plated 3D printed waveguide part, (b) a patterned bottom side of the PCB that mates with the waveguide part, (c) full assembly circuit. Total transition length is 30.4 mm (8.2 mm + 1mm on PCB's top metal), total printed part length is 84.8 mm, total PCB length is 98.8 mm.

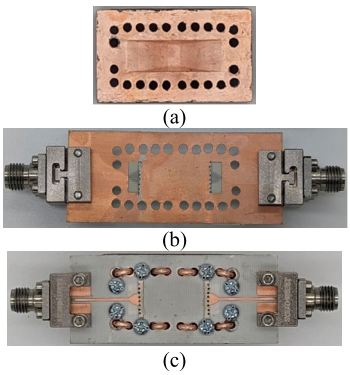

FIGURE 5. Photographs of the fabricated TR-28 transition in back-to-back configuration: (a) copper-plated 3D printed waveguide part, (b) a patterned bottom side of the PCB that mates with the waveguide part, (c) full assembly circuit. Total transition length is 9.3 mm (2.5 mm + 1mm on PCB's top metal), total printed part length is 35.6 mm, total PCB length is 49.6 mm.

different behavior between the microstrip and the waveguide ports is observed as expected. Insertion loss is 0.71 dB @ f_{0_WR90} and 0.59 dB @ f_{0_WR28} as a lossy substrate is present only up to 0.27 l_{tap}. Most of the loss is attributed to the (suspended) microstrip region dielectric losses and a total of conductor losses. The performance is very good considering assumptions made for the sake of geometry generation and no EM-based geometry optimization was done whatsoever.

Transitions demonstrators were fabricated and their photographs are provided in Fig. 4 and Fig. 5. Importantly, the top metal plane was removed outside the transition area (with 1 mm extension past via circumference) to demonstrate the real-estate availability advantage of the proposed geometries.

The transition was arranged in a back-to-back configuration with a microstrip being the interface for VNA while a

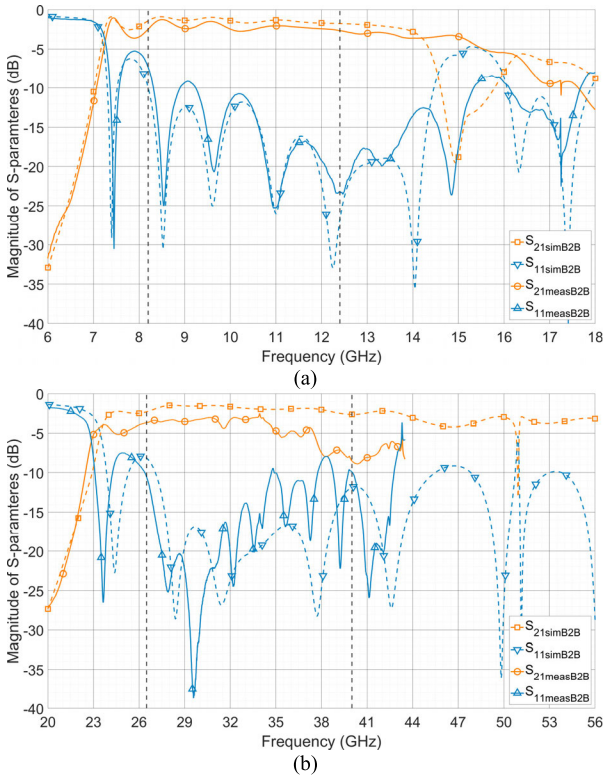

FIGURE 6. Measured S-parameters of the fabricated (a) TR-90 and (b) TR-28 transition demonstrator (solid lines) along with EM simulated data (dashed lines) overlaid. WG TE10 bandwidth marked (vertical dashed lines).

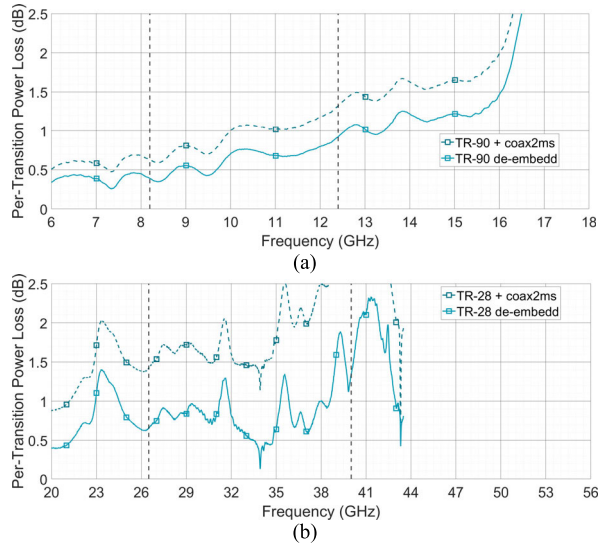

FIGURE 7. Calculated per-transition power loss of the (a) TR-90 and (b) TR-28 demonstrators with coax-to-MS transitions loss de-embedded (solid lines) and as measured (dashed lines). WG TE10 bandwidth marked (vertical dashed lines).

short, roughly quarter wave long @ f_0 section of waveguide (10 mm in TR-90, 3 mm in TR-30) was added in-between to bridge the halves. Such an arrangement is very convenient to measure while maintaining the bandwidth and loss information of the transition. The relation between a single transition S_{21trab} and a back-to-back S_{21b2b} with a transmission line interconnect (γl), assuming good matching is $S_{21b2b} = S_{21tran}^2 e^{\gamma l}$ hence, twice the single transition response with extra phase shift and attenuation of the interconnect. The transitions' top metal pattern was supplemented on each transition side with a short section of a coplanar waveguide to microstrip transition for smoother launching the TEM wave from the Southwest Microwave 3.5 mm coax screw-on end-launch connectors making the MS line 14 mm long in total. Therefore, an extra Thru PCB (coax-to-microstrip in back-to-back configuration) was fabricated to de-embed power losses of the above launchers as they are a significant contributor while the hybrid waveguide section can be ignored.

The measured S-parameters of the TR-90 and TR-28 demonstrators are provided in Fig. 6 along with EM simulation data overlaid (a full-wave model used for transition design verification supplemented with surface roughness and contact resistance data of Section II.C) while calculated per-transition total power loss (TPL) is shown in Fig. 7. As seen from S-parameters, the performance of the fabricated circuit fairly matches the simulations with the discrepancy being mainly attributed to fabrication and assembly finite accuracy with TR-28 being more affected due to smaller absolute dimensions. An average de-embedded per-transition TPL is ~0.63 dB (0.94 dB embedded) within the WR-90 nominal bandwidth and ~0.86 dB (1.92 dB embedded) within the WR-28 one. An increased TPL slope is observed in the case of TR-90 above 15 GHz due to the propagation of a more lossy higher-order waveguide mode. For TR-28 this is not visible due frequency limited measured data. The measured bandwidth BW (f_u/f_l) @ 10 dB of impedance match is 1.85 for TR-90 and 1.43 for TR-28. It is seen, however, that impedance matching, and bandwidth could be improved by applying optional EM-based transition layout optimization, using broadband measurement-based substrate permittivity, and accounting at CAM files preparation stage for post-curing polymer shrinkage, metal thickness etc.

To identify the assembly impact on the above TPL results, an EM simulation-based analysis was carried out on an example of TR-90. The affection of PCB vs. 3D printed part alignment, as well as increased contact resistance and air gaps, influenced was studied. For alignment, a standard PCB fabrication has a typical accuracy of ±0.1 mm for hole diameter and ± 0.1mm for hole position while a typical M-SLA printer has a resolution in XY of 0.05 mm. Tighter tolerances can also be obtained easily at increased fabrication cost. A worst-case scenario of a two-point alignment with a deviation of $\Delta x = +0.25$ mm and $\Delta y = +0.25$ mm was assumed. The in-band TPL deviated by ±0.05 dB with little to no effect on return loss level. For contact resistance, an earlier identified surface resistance was compared against a lossless contacting surface. For the lossy case, the in-band TPL increased by 0.2 dB to 0.3 dB while the return loss level improved by 0.4 dB to 0.5 dB. Finally, for air gaps, a scenario of PCB deflection due to discussed high-no clamping pattern leading to an air gap of 50 μm at half-width of screws pitch was assumed. As a result, the in-band TPL increased

TABLE 1. Summary of the properties and measured performance of various microstrip-to-waveguide transitions.

Ref.	Transition type	Feed vs. WG	Geometry generation	Vias	Loss per tran.# (dB)	l x w (mm) / λ_g (mm)[&]; l/λ_g (mm/mm)	BW* f_h/f_l	WG fabric.	Freq. band
[12]	Continuous impedance transformer	Inline	Mixed analytic full-wave	yes	~0.6	8.18 x 15.8 / 25.04; *0.33*	>1.5	E-SIW	Ku (WR-62)
[13]	Stepped impedance transformer	Inline	Mixed analytic full-wave	yes	-	12.25 x 3.51 / 11.66; *1.05*	> 1.5	multilayer E-SIW	Ka (WR-28)
[19]	Quasi-yagi antenna feeding	Inline	Full-wave optimization	no	0.9 @ f_0	11.47 x 10.16 / 36.55; *0.31*	~1.55	MM	X (WR-90)
[20]	Through probe coupling	Perpend.	Full-wave optimization	yes	0.6 – 0.9	9.56 x 7.11 / 11.66; *0.82*	~1.2	MM	Ka (WR-28)
[21]	Stepped impedance transformer	Inline	Full-wave optimization	no	0.75 – 1.5	7.9 x 3.1 / 5.23; *14.6*	~1.05	MM	E (WR-12)
[23]	Through patch coupling	Perpend.	Full-wave optimization	yes	0.4 – 2	2.8 x 4.8 / 5.23; *0.54*	~1.2	MM	E (WR-12)
[24]	Stepped impedance transformer	Inline	Fast analytic	no	~0.6	4.79 x 2.54 / 4.2; *1.14*	> 1.4	MM	W (WR-10)
[25]	Through patch coupling	Parallel	Full-wave optimization	no	1.1 – 2.0	15.2 x 22.86/ 36.55; *0.42*	1.4	C3Dp[+]	X (WR-90)
[25]	Through patch coupling	Parallel	Full-wave optimization	no	1.7 – 3.9	6.2 x 10.67/ 17.38; *0.36*	1.46	C3Dp[+]	K (WR-42)
[26]	Through probe coupling	Parallel	Full-wave optimization	yes	< 1.1 dB	14.1 x 22.86 / 36.55; *0.39*	1.8	C3Dp[+%]	X (WR-90)
This TR-90	Continuous impedance transformer	Parallel	Fast analytic	yes	0.4 – 1.3	30.4 (9.2 on top metal) x 22.86 / 36.55; *0.83 (0.25)*	~1.9	C3Dp[+]	X (WR-90)
This TR-28	Continuous impedance transformer	Parallel	Fast analytic	yes	0.7 – 1.7	9.3 (3.5 on top metal) x 7.11 / 11.66; *0.8 (0.3)*	~1.4	C3Dp[+]	Ka (WR-28)

*Bandwidth where Return Losses are better than 10 dB; [&]Transition`s length l by width w/ guided wavelength λ_g at WG band center; wavelength normalized length l/λ_g; [#]feeding line length varies among reported designs; MM – all-metal milling, C3Dp – metal coated 3D print; [+]the same fabrication scheme used; [%]requires selective 3D print metallization.

by 0.05 dB while the return loss level improved by 2.5 dB to 4 dB. In summary, applying sufficient clamping force that ensures a good galvanic contact between on-PCB and on-print metal surfaces is of great importance as to maintain low power losses.

The proposed transitions were finally compared with other solutions in the literature and a summary is provided in Table 1. The transition in [12] uses a smooth impedance transformer in the form of a tapered dielectric insert into air-filled E-SIW that requires precision milling and vertical wall metallization along with conductively bonded extra laminates with metal planes acting as top and bottom E-SIW conductor what requires a sophisticated, hence costly PCB process. The transition in [13] uses a step transformer where each step requires an extra layer in a multilayer PCB stack apart from precision milling, vertical wall metallization, and precise assembly that ensures the galvanic connection between metals on each laminate; the above not only restricts geometrical flexibility but also highly increases fabrication cost similarly as in the former case. The transition proposed in [25] features narrower bandwidth due to the resonant nature of the through patch coupling and high-power losses, mainly due to radiation of the open-ended microstrip stub; the transition shown in [26] improves the bandwidth at the expense of requirement for selectively metal coated thin radiation probe to be integrated within the 3D printed shell but still the bandwidth is lower, impedance match worse and power losses higher that in this work. On the other hand, it is seen, that the integrated waveguide and the proposed transition feature fast geometry generation procedure, easy integration with PCBs, high design flexibility, compact size (fabricated demonstrators occupy on PCB's top metal only ~0.3 mm/mm guided wavelength normalized length), low-cost realization due to the use of AM process, very wide operational bandwidth, and low insertion losses. The above features make the proposed approach well-suited for implementation in the next generation of highly integrated cm- and mm-wave circuits.

IV. CONCLUSION

A novel type of highly integrated low-loss stack-up was studied in detail that leverages additive manufacturing for integration of a 3D printed and metal-coated air-filled waveguide with a Printed Circuit Board (PCB) by sharing a common ground plane. A complimentary microstrip to waveguide transition was proposed that takes advantage of the flexibility of 3D-printing to implement a smooth taper ensuring wideband impedance transformation between the guides with matched E-field orientation for minimized losses. The design procedure is provided and validated that requires no EM optimization yet yields sufficient performance. An integrated waveguide and two transition demonstrators were manufactured confirming the superior performance of the proposed solution while requiring inexpensive fabrication technologies. It was shown that the transition can occupy a relatively small area on the top on-PCB metal layer thus leaving plenty of space for other active and passive components leading to

a very compact layout. The experimental study validated the proposed broadband transition implementation as to be suited for implementation in the next generation of highly integrated and high-performance microwave and mm-wave circuits.

APPENDIX

The design of the proposed transition requires the realization of a given impedance taper along its length. To allow fast geometry calculation, one can employ analytical formulas to calculate each guide's impedance. Cross-sectional views of the discussed guides are shown in Fig. 1c.

Suspended microstrip

The characteristic impedance Z_{sMS} is derived from the impedance Z_0 of the microstrip in a homogenous medium, and the static TEM effective dielectric constant $\varepsilon_{eff}(0)$ at zero frequency [35]:

$$Z_{sMS} = \frac{Z_0}{\sqrt{\varepsilon_e(0)}} \tag{A.1}$$

where Z_0 is given by e.g. [36].

Dielectric-Loaded and Air-Filled Waveguide

The wave impedance Z_{dlWG} for the TE mode is based on power-current definition [37] as it enables incorporating the narrow-wall height, and the effective dielectric constant ε_{eff} of the dielectric stack-up:

$$Z_{dlWG} = \frac{k}{\beta}\eta_0\sqrt{\frac{1}{\varepsilon_{eff}}}\frac{\pi^2}{8}\frac{(h_{WG}+h_{WG})}{w_{WG}} \tag{A.2}$$

where η_0 is the wave impedance of vacuum. The effective permittivity of a dielectric block composed of two layers having permittivity and thickness of ε_{sub}, h_{sub}, and $\varepsilon_{WG} = 1$, h_{WG} respectively can be calculated through an analogy to a series arrangement of parallel capacitors as:

$$\frac{1}{\varepsilon_{eff}} = \frac{1}{\varepsilon_{sub}}\frac{h_{sub}}{h_{sub}+h_{WG}} + \frac{1}{\varepsilon_{WG}}\frac{h_{WG}}{h_{sub}+h_{WG}} \tag{A.3}$$

Air-Filled Waveguide

The wave impedance Z_{afWG} derived from A.2 for $\varepsilon_{eff} = 1$:

$$Z_{afWG} = \frac{k}{\beta}\eta_0\frac{\pi^2}{8}\frac{h_{WG}}{w_{WG}} \tag{A.4}$$

REFERENCES

[1] R. Sorrentino and O. A. Peverini, "Additive manufacturing: A key enabling technology for next-generation microwave and millimeter-wave systems [point of view]," *Proc. IEEE*, vol. 104, no. 7, pp. 1362–1366, Jul. 2016.

[2] S. A. Nauroze, J. G. Hester, B. K. Tehrani, W. Su, J. Bito, R. Bahr, J. Kimionis, and M. M. Tentzeris, "Additively manufactured RF components and modules: Toward empowering the birth of cost-efficient dense and ubiquitous IoT implementations," *Proc. IEEE*, vol. 105, no. 4, pp. 702–722, Apr. 2017.

[3] R. Bahr, B. Tehrani, and M. M. Tentzeris, "Exploring 3-D printing for new applications: Novel inkjet- and 3-D-printed millimeter-wave components, interconnects, and systems," *IEEE Microw. Mag.*, vol. 19, no. 1, pp. 57–66, Jan. 2018.

[4] A. Tamayo-Dominguez, J.-M. Fernandez-Gonzalez, and M. Sierra-Perez, "Metal-coated 3D-printed waveguide devices for mm-wave applications [application notes]," *IEEE Microw. Mag.*, vol. 20, no. 9, pp. 18–31, Sep. 2019.

[5] M. I. M. Ghazali, S. Karuppuswami, A. Kaur, and P. Chahal, "3D printed high functional density packaging compatible out-of-plane antennas," *Additive Manuf.*, vol. 30, Dec. 2019, Art. no. 100863.

[6] M. D'Auria, W. J. Otter, J. Hazell, B. T. W. Gillatt, C. Long-Collins, N. M. Ridler, and S. Lucyszyn, "3-D printed metal-pipe rectangular waveguides," *IEEE Trans. Compon., Packag., Manuf. Technol.*, vol. 5, no. 9, pp. 1339–1349, Sep. 2015.

[7] J. Kuhling, R. Dahle, D. Chowdhry, and P. Laforge, "Applying additive manufacturing to integrate coaxial connectors with 3D printed waveguides for cascaded RF link applications," *Additive Manuf.*, vol. 35, Oct. 2020, Art. no. 101280.

[8] E. López-Oliver, C. Tomassoni, L. Silvestri, M. Bozzi, L. Perregrini, S. Marconi, G. Alaimo, and F. Auricchio, "3-D-printed compact bandpass filters based on conical posts," *IEEE Trans. Microw. Theory Techn.*, vol. 69, no. 1, pp. 616–628, Jan. 2021.

[9] J. D. Martinez, S. Sirci, V. E. Boria, and M. A. Sanchez-Soriano, "When compactness meets flexibility: Basic coaxial SIW filter topology for device miniaturization, design flexibility, advanced filtering responses, and implementation of tunable filters," *IEEE Microw. Mag.*, vol. 21, no. 6, pp. 58–78, Jun. 2020.

[10] X.-P. Chen and K. Wu, "Substrate integrated waveguide filters: Design techniques and structure innovations," *IEEE Microw. Mag.*, vol. 15, no. 6, pp. 121–133, Sep. 2014.

[11] K. Wu, M. Bozzi, and N. J. G. Fonseca, "Substrate integrated transmission lines: Review and applications," *IEEE J. Microw.*, vol. 1, no. 1, pp. 345–363, Jan. 2021.

[12] H. Esteban, A. Belenguer, J. R. Sánchez, C. Bachiller, and V. E. Boria, "Improved low reflection transition from microstrip line to empty substrate-integrated waveguide," *IEEE Microw. Wireless Compon. Lett.*, vol. 27, no. 8, pp. 685–687, Aug. 2017.

[13] J. A. Martínez, A. Belenguer, J. J. De Dios, H. E. González, and V. E. Boria, "Wideband transition for increased-height empty substrate integrated waveguide," *IEEE Access*, vol. 7, pp. 149406–149413, 2019.

[14] A. Belenguer, H. Esteban, A. L. Borja, and V. E. Boria, "Empty SIW technologies: A major step toward realizing low-cost and low-loss microwave circuits," *IEEE Microw. Mag.*, vol. 20, no. 3, pp. 24–45, Mar. 2019.

[15] K. Y. Kapusuz, S. Lemey, and H. Rogier, "Substrate-independent microwave components in substrate integrated waveguide technology for high-performance smart surfaces," *IEEE Trans. Microw. Theory Techn.*, vol. 66, no. 6, pp. 3036–3047, Jun. 2018.

[16] G. Savvides, N. Duangrit, N. Chudpooti, P. Akkaraekthalin, U. Imberg, I. D. Robertson, and N. Somjit, "3D rapid-prototyped 21–31-GHz hollow SIWs for low-cost 5G IoT and robotic applications," *IEEE Access*, vol. 9, pp. 11750–11760, 2021.

[17] H.-W. Yao, A. Abdelmonem, J.-F. Liang, and K. A. Zaki, "Analysis and design of microstrip-to-waveguide transitions," *IEEE Trans. Microw. Theory Techn.*, vol. 42, no. 12, pp. 2371–2380, Dec. 1994.

[18] M. Simone, A. Fanti, G. Valente, G. Montisci, R. Ghiani, and G. Mazzarella, "A compact in-line waveguide-to-microstrip transition in the Q-band for radio astronomy applications," *Electronics*, vol. 7, no. 2, p. 24, Feb. 2018.

[19] N. Kaneda, Y. Qian, and T. Itoh, "A broad-band microstrip-to-waveguide transition using quasi-Yagi antenna," *IEEE Trans. Microw. Theory Techn.*, vol. 47, no. 12, pp. 2562–2567, Dec. 1999.

[20] A. Mozharovskiy, S. Churkin, A. Arternenko, and R. Maslcnnikov, "Wideband probe-type waveguide-to-microstrip transition for 28 GHz applications," in *Proc. 48th Eur. Microw. Conf. (EuMC)*, Madrid, Spain, Sep. 2018, pp. 113–116.

[21] B. Boukari, E. Moldovan, S. Affes, K. Wu, R. G. Bosisio, and S. O. Tatu, "Robust microstrip-to-waveguide transitions for millimeter-wave radar sensor applications," *IEEE Antennas Wireless Propag. Lett.*, vol. 8, pp. 759–762, 2009.

[22] X. Huang and K.-L. Wu, "A broadband U-slot coupled microstrip-to-waveguide transition," *IEEE Trans. Microw. Theory Techn.*, vol. 60, no. 5, pp. 1210–1217, May 2012.

[23] N. Thanh Tuan, K. Sakakibara, and N. Kikuma, "Bandwidth extension of planar microstrip-to-waveguide transition by controlling transmission modes through via-hole positioning in millimeter-wave band," *IEEE Access*, vol. 7, pp. 161385–161393, 2019.

[24] J. Pérez-Escudero, A. Torres-García, R. Gonzalo, and I. Ederra, "A simplified design inline microstrip-to-waveguide transition," *Electronics*, vol. 7, no. 10, p. 215, Sep. 2018.

[25] J. Sorocki, I. Piekarz, A. Samulak, N. Delmonte, L. Silvestri, S. Marconi, G. Alaimo, F. Auricchio, and M. Bozzi, "Additively fabricated air-filled waveguide integrated with printed circuit board using a through-patch transition," *IEEE Microw. Wireless Compon. Lett.*, vol. 31, no. 11, pp. 1207–1210, Nov. 2021.
[26] I. Piekarz, J. Sorocki, N. Delmonte, L. Silvestri, S. Marconi, G. Alaimo, F. Auricchio, and M. Bozzi, "Wideband microstrip to 3-D-printed air-filled waveguide transition using a radiation probe," *IEEE Microw. Wireless Compon. Lett.*, vol. 32, no. 10, pp. 1179–1182, Oct. 2022.
[27] R. Klopfenstein, "A transmission line taper of improved design," *Proc. IRE*, vol. 44, no. 1, pp. 31–35, Jan. 1956.
[28] D. Pozar, *Microwave Engineering*, 4th ed. Hoboken, NJ, USA: Wiley, 2012.
[29] J. E. Rayas-Sanchez and V. Gutierrez-Ayala, "A general EM-based design procedure for single-layer substrate integrated waveguide interconnects with microstrip transitions," in *IEEE MTT-S Int. Microw. Symp. Dig.*, Atlanta, GA, USA, Jun. 2008, pp. 983–986.
[30] E. O. Hammerstad and F. Bekkadal, "A microstrip handbook," Electron. Res. Lab., Univ. Trondheim, Norway, ELAB Rep. STF44 A74169, Feb. 1975.
[31] J. Sorocki, K. Wincza, S. Gruszczynski, and I. Piekarz, "Study on 3D printed snap-fit joints for assembly of PCB-integrated additively fabricated air-filled waveguide," in *Proc. 52nd Eur. Microw. Conf. (EuMC)*, Milan, Italy, Sep. 2022, pp. 274–277.
[32] *Keysight Vector Network Analyzer Uncertainty Calculator Software*. Accessed Jun. 1, 2023. [Online]. Available: https://www.keysight.com/es/en/lib/software-detail/computer-software/downloadable-vector-network-analyzer-uncertainty-calculator-1000000418epsgsud.html
[33] J. Sorocki and I. Piekarz, "Low-cost microwave components' fabrication in hybrid technology of laminates and additive manufacturing on an example of miniaturized suspended directional coupler," *IEEE Access*, vol. 8, pp. 128766–128775, 2020.
[34] J. Shen, M. Aiken, C. Ladd, M. D. Dickey, and D. S. Ricketts, "A simple electroless plating solution for 3D printed microwave components," in *Proc. Asia–Pacific Microw. Conf. (APMC)*, Dec. 2016, pp. 1–4.
[35] P. Pramanick and P. Bhartia, "Computer-aided design models for millimeter-wave finlines and suspended-substrate microstrip lines," *IEEE Trans. Microw. Theory Techn.*, vol. MTT-33, no. 12, pp. 1429–1435, Dec. 1985.
[36] E. Hammerstad and O. Jensen, "Accurate models for microstrip computer-aided design," in *IEEE MTT-S Int. Microw. Symp. Dig.*, Mar. 1980, pp. 407–409.
[37] T. Djerafi, A. Doghri, and K. Wu, "Substrate integrated waveguide antennas," in *Handbook of Antenna Technologies*, Z. Chen, Eds. Singapore: Springer, 2015.

JAKUB SOROCKI (Senior Member, IEEE) received the M.Sc., Ph.D., and D.Sc. degrees in electrical engineering from the AGH University of Krakow, Kraków, Poland, in 2013, 2018, and 2023, respectively.

Since 2011, he has been cooperating with the Microwave Research Group, Institute of Electronics, AGH University of Krakow. In 2012, he was a Visiting Student with the Ilmenau University of Technology, Ilmenau, Germany. In 2017, he was a Visiting Post-Graduate Researcher with Michigan State University, East Lansing, MI, USA. In 2019, he was a Systems Engineer of ADAS mm-wave radars in the automotive industry. From 2020 to 2021, he was a Visiting Postdoctoral Researcher with the University of Pavia, Pavia, Italy. In 2023, he was a Visiting Postdoctoral Researcher with the Autonomous University of Barcelona, Barcelona, Spain. Since 2023, he has been an Associate Professor with AGH University of Krakow. His research interests include the development of low-loss and high-performance microwave circuits in waveguide and strip transmission line technique for industrial applications taking advantage of additive and subtractive fabrication technologies.

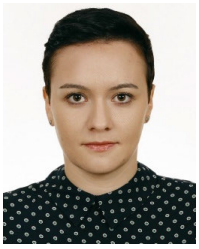

ILONA PIEKARZ (Senior Member, IEEE) received the M.Sc., Ph.D., and D.Sc. degrees in electrical engineering from the AGH University of Krakow, Kraków, Poland, in 2013, 2018, and 2023, respectively.

Since 2011, she has been cooperating with the Microwave Research Group, Institute of Electronics, AGH University of Krakow. In 2012, she was a Visiting Student with the Ilmenau University of Technology, Ilmenau, Germany. In 2017, she was a Visiting Post-Graduate Researcher with Michigan State University, East Lansing, MI, USA. In 2019, she was a Systems Engineer of ADAS mm-wave radars in the automotive industry. From 2020 to 2021, she was a Visiting Postdoctoral Researcher with the University of Pavia, Pavia, Italy. In 2023, she was a Visiting Postdoctoral Researcher with the Autonomous University of Barcelona, Barcelona, Spain. Since 2023, she has been an Associate Professor with AGH University of Krakow. Her research interests include the development of sensors and measurement systems in strip transmission line techniques for industrial and biomedical applications that take advantage of both subtractive and additive fabrication techniques.

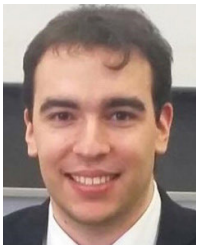

NICOLO DELMONTE (Member, IEEE) was born in Broni, Italy, in 1992. He received the bachelor's degree in electronics and computer engineering and the master's degree in electronic engineering from the University of Pavia, Italy, in February 2015 and September 2017, respectively, and the Ph.D. degree from the Microwave Laboratory, in 2020. His research interests include microwave components in substrate integrated waveguide (SIW) technology and RF circuit design.

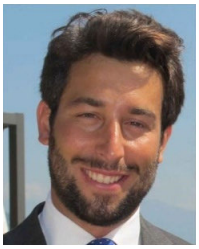

LORENZO SILVESTRI (Member, IEEE) was born in Novara, Italy, in July 1987. He received the M.Sc. degree in electronic engineering–telecommunication system curriculum and the Ph.D. degree in electronic, electrical and computer engineering from the University of Pavia, Pavia, Italy, in 2014 and 2019, respectively.

After the Ph.D. until September 2020, he held a postdoctoral position with the University of Pavia, involved on the design of reconfigurable SIW antennas. He is currently a Researcher with the University of Pavia. In 2014, he was a recipient of the One-Year Post-Graduate Scholarship at the University of Pavia, involved on passive Substrate Integrated Waveguide (SIW) Component. In 2015, he was a co-recipient of the Best Paper Award at 15th Mediterranean Microwave Symposium (MMS 2015).

MAURIZIO BOZZI (Fellow, IEEE) received the Ph.D. degree in electronics and computer science from the University of Pavia, Pavia, Italy, in 2000.

He is currently a Full Professor of electromagnetic with the University of Pavia. His research interests include computational electromagnetics, substrate integrated waveguide technology, and the use of novel materials and fabrication technologies for microwave circuits. He is the 2024 President of the IEEE Microwave Theory and Technology Society (MTT-S).